Filament formation via the instability of a stretching viscous sheet: Physical mechanism, linear theory, and fiber applications

Bingrui Xu,[1] Minhao Li,[1] Feng Wang,[1] Steven G. Johnson,[2] Yoel Fink,[3,4] and Daosheng Deng[1,*]

[1]*Department of Aeronautics and Astronautics, Fudan University, Shanghai, 200433, China*

[2]*Department of Mathematics, Massachusetts Institute of Technology, Cambridge, Massachusetts 02139, USA*

[3]*Department of Materials Science and Engineering, Massachusetts Institute of Technology, Cambridge, Massachusetts 02139, USA*

[4]*Research Laboratory of Electronics, Massachusetts Institute of Technology, Cambridge, Massachusetts 02139, USA*

(Received 23 February 2018; revised manuscript received 30 July 2018; published 8 July 2019)

Many intriguing patterns are driven by fluid instabilities, even down to micrometer and nanometer scales, with numerous technological and industrial applications. Here, we propose a novel physical mechanism for filament formation in a stretched viscous sheet by combining stretching and van der Waals forces. We show that a transverse instability is enhanced while the longitudinal instability is suppressed, resulting in filamentation. We find a close agreement between the experimental data and the predictions of a linear-stability analysis. These results offer a pathway to achieving sophisticated microstructuring–nanostructuring for functional devices in either a single fiber or in integrated fabrics for large-scale textiles.

DOI: 10.1103/PhysRevFluids.4.073902

I. INTRODUCTION

Liquid sheets are ubiquitous in nature at both small scales (such as tear films in eyes) and large scales (such as flows of continental ice sheets in geology), while being essential for many industrial applications (including painting, coating, microfluidics, and manufacturing of glass and plastics) [1,2]. Instability of liquid sheets can be observed in a host of fascinating patterns. For example, a moving sheet disintegrates into droplets due to an inertial effect [3,4]. A viscous sheet experiencing an external force undergoes buckling, coiling, or wrinkling instabilities [5–8]. In addition, as thickness is decreased down to hundreds of nanometers and the van der Waals force (London dispersion force) begins to play a dominant role, a sheet driven by spinodal dewetting spontaneously ruptures into a random array of droplets [9,10].

Recently, another instability has been identified when a viscous sheet, subjected to a unidirectional stretching, evolves into an array of continues filaments arranged orderly during a process of thermal drawing [11,12]. This pattern, an array of continuous filaments, is unlike that of other fluid instabilities that typically produced droplets (for example, in spinodal dewetting of a thin sheet or in capillary-instability breakup of a cylindrical jet). In this phenomenon, stability is preserved along the longitudinal (stretching) direction, while instability occurs exclusively along the transverse (perpendicular to the stretching) direction. Therefore, we use the term "anisotropic instability of a stretching viscous sheet" (AISVS) for this physical phenomenon.

*dsdeng@fudan.edu.cn

Indeed, much progress has been made to address the physical mechanism of AISVS. For example, as a heuristic model, a fluid-front instability was proposed, but the prerequisite presence of a specific cylindrical shape for the fluid front was ambiguous [11]. A simple geometrical argument might explain the preferential instability along the transverse direction, but the mechanism of instability was obscure [13]. Moreover, van der Waals forces might be relevant at these scales, but the effect of stretching was neglected and the source or longitudinal stability was still unclear [14]. Thus, the underlying mechanism remains perplexing and needs to be further elucidated. Nevertheless, the observation of AISVS has inspired interdisciplinary research to utilize fluid instabilities in fibers, such as in-fiber nanostructures manufactured via capillary instabilities [15,16].

In this paper, we propose a physical mechanism for AISVS by taking into account both van der Waals forces and the effect of stretching. By employing linear stability analysis and performing numerical calculations, we find that the transverse instability is enhanced while the longitudinal instability is suppressed. The theoretical predictions agree remarkably well with experiments for fiber systems.

This paper is organized as follows. In Sec. II, a general physical mechanism for AISVS is briefly proposed. In Sec. III, a mathematical model is presented: describing the effect of stretching and the changes of sheet shape (Sec. III A), building linear theory of the dewetting instability of a sandwiched sheet with a uniform thickness arising from the van der Waals force (Sec. III B), and finally obtaining the total growth rate by integrating local growth rates to take into account the stretching effect (Sec. III C). Then, in Sec. IV, numerical predictions of anisotropic instabilities in stretching sheets are studied by comparing the total growth rates of perturbations along the transverse and longitudinal directions. Moreover, in Sec. V, the proposed model is applied to thermal drawing to understand the observed instability and breakup. Last, we conclude in Sec. VI with a summary and a discussion of the future opportunities for AISVS.

II. PHYSICAL MECHANISM

Let us begin with a qualitative discussion of a possible mechanism for the transverse instability and the longitudinal stability in AISVS, and summarize the key parameters. First, since AISVS was observed at the microscopic length scale, van der Waals forces should become significant and may lead to the transverse instability, similar to dewetting phenomena. Secondly, we conjecture that the effect of stretching for a sheet might be analogous to that of a continuous falling viscous jet under gravity, and hence the longitudinal instability is suppressed [17]. In thermal drawing, a cylindrical preform (a thin glass sheet in a polymer matrix) is heated into a viscous state and stretched by a drawing force as shown in Fig. 1(a). For the typical geometrical parameters, the radii of interfaces are $2R_1 \sim 2R_2 \sim R_3 \sim 1$ cm at the inlet, while the thickness are $H_0 = R_2 - R_1 < 10$ μm and the stretching length is $L > 10$ cm (the ratio between initial film thickness and stretching length, $\varepsilon = H_0/L = 10^{-4} \ll 1$) [11,12]. The viscosity μ_2 of glass sheet varies from 1 to 10^5 Pa s, while the polymer viscosity μ_1 is about 10^5 Pa s [11,12]. Since the radii are so much larger than the layer thicknesses, we can simplify our model of thermal drawing [Fig. 1(a)] by neglecting the curvature effect, approximating the cylindrical geometry by three-layer liquid sheets: a viscous sheet with initial thickness H_0 sandwiched within another fluid, stretched over a length L [Fig. 1(b)]. Our proposed mechanism of AISVS is illustrated in Fig. 1(c): (i) a viscous sheet undergoes elongation deformation when subjected to stretching; (ii) perturbations are amplified by a transverse instability; (iii) because of stretching, the longitudinal stability persists. Consequently, this anisotropic instability results in an array of filaments.

III. MATHEMATICAL MODEL

We consider a viscous liquid sheet with viscosity μ_2, thickness H_0, velocity w_0, and width $2\ell_0 = 2\pi R_1$ at the inlet, sandwiched within another fluid of high viscosity μ_1, that is stretched by a drawing force over a length L to the take-up speed w_f, as seen in Fig. 1(b). The drawing ratio can be described

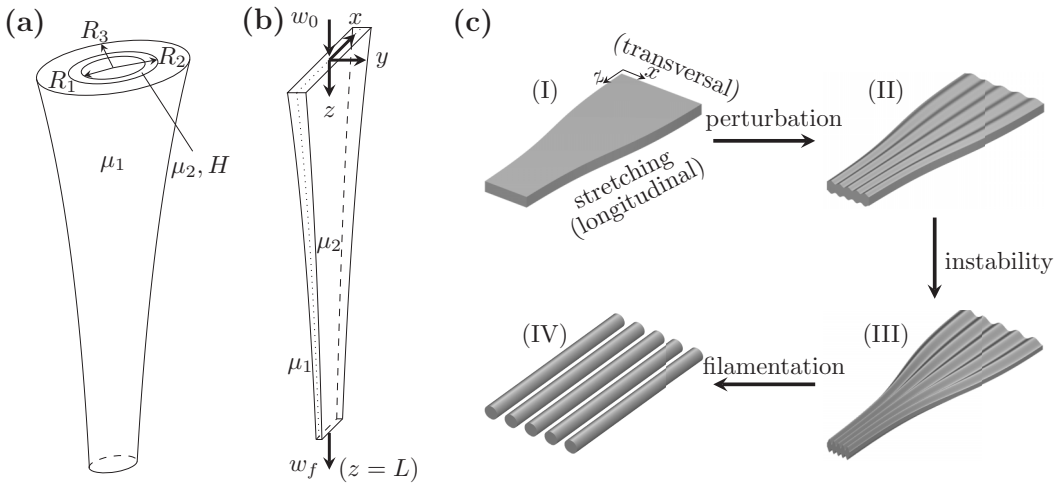

FIG. 1. Physical mechanism. (a) Sketch of thermal drawing. A cylindrical preform, composed by a thin glass sheet in a polymer matrix, is heated into viscous fluid and stretched into fibers, resulting in the axial extension and transverse shrinkage. For the typical geometrical parameters, the radii of interfaces $2R_1 \sim 2R_2 \sim R_3 \sim 1$ cm at the inlet, while the thickness $H_0 = R_2 - R_1 < 10$ μm and the stretching length $L > 10$ cm. Due to $H_0 \ll R_1$, the curvature effect of cylindrical structures can be neglected. (b) Sketch of three-layer liquid sheets. A stretching sheet (viscosity μ_2, an initial width $2\ell_0 = 2\pi R_1$) sandwiched by liquid with viscosity μ_1. An initial velocity w_0, and the final velocity w_f out of the stretching region. (c) Sketch for the mechanism of AISVS, where the transverse direction is along x while the longitudinal direction is along z.

by the final scaling factor $S_f \equiv (w_f/w_0)^{1/2}$, an experimental parameter. The coordinates are chosen so that the x axis is parallel to the width, the y axis is parallel to the thickness, and z axis is parallel to the flow (stretching) direction, with the origin located in the midplane of the liquid sheet.

Using the thin-film assumption $\varepsilon \ll 1$ and neglecting the inertia (the Reynolds number $\mathrm{Re} \ll 1$ during thermal drawing [11,13]), gravity, and surface tension (negligible with respect to the drawing force), the Stokes equations and continuity equations reduce to a two-dimensional system of evolution equations for the sheet thickness $H = H(x, z)$ and in-plane velocities $u = u(x, z)$ and $w = w(x, z)$ [6,18],

$$\partial_t H + \partial_x(uH) + \partial_z(wH) = 0, \tag{1a}$$

$$\partial_x(H\sigma_{xx}) + \partial_z(H\sigma_{xz}) = 0, \tag{1b}$$

$$\partial_x(H\sigma_{xz}) + \partial_z(H\sigma_{zz}) = 0. \tag{1c}$$

with the stress tensor components $\sigma_{xx} = 2\mu_2(2\partial_x u + \partial_z w)$, $\sigma_{zz} = 2\mu_2(\partial_x u + 2\partial_z w)$, $\sigma_{xz} = \mu_2(\partial_x w + \partial_z u)$. As the sheet thickness varies slowly in the longitudinal direction ($\varepsilon \ll 1$), the growth of perturbations can be treated by a local analysis in which H is taken to be nearly constant, as discussed below.

A. Lateral shape of a stretching sheet in the steady state

A stretching thin sheet with evolution Eqs. (1) has been thoroughly studied for various ratios $a = \ell/H$ of half width ℓ to length H by Scheid [18]; in thermal drawing, the ratio is $a = \pi R_1/L \approx 0.15$. In particular, the shape of stretching sheet in the steady state can be obtained by following Scheid's method [18] to solve the evolution equations (1) with the time derivatives set to zero. In Fig. 2, the attenuation rates of thickness $S_H = H_0/H$ and width $S_\ell = \ell_0/\ell$ along the sheet are depicted at the final scaling factor $S_f = 10$.

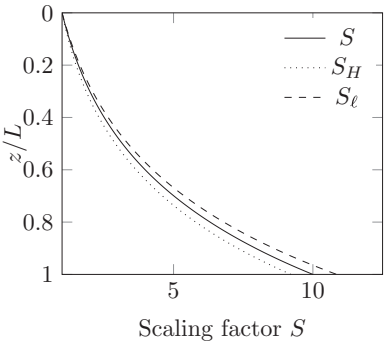

FIG. 2. The attenuation rates of thickness $S_H = H_0/H$ (dotted line) and width $S_\ell = \ell_0/\ell$ (dashed line) along the sheet and their approximate scale factor S (solid line) in the "fiber limit" case at the final scaling factor $S_f = 10$ and the ratio $a = \pi R_1/L = 0.15$.

According to Scheid's study [18], there is a one-dimensional "fiber limit" case, when the width is as small as the thickness. In this case, the transverse stress is $\sigma_{zz} = 0$ and the evolution equations are [18]

$$w\ell H = \text{const}, \quad 3\mu_2 \ell H \partial_z w = \text{const}. \tag{2}$$

From the above Eq. (2), the velocity is

$$w(z) = w_0 \exp\left(\frac{z}{L} \ln \frac{w_f}{w_0}\right). \tag{3}$$

Consequently, In the fiber limit, the width and thickness of the sheet are attenuated in the same proportion $S = H_0/H = \ell_0/\ell$ given by

$$S(z) \equiv (w/w_0)^{1/2} = \exp\left(\frac{z}{L} \ln S_f\right). \tag{4}$$

This scale factor S at $S_f = 10$ in the fiber limit is shown in Fig. 2, along with exact solutions for the attenuations $S_H = H_0/H$ and $S_\ell = \ell_0/\ell$ from the full two-dimensional Eqs. (1) at $a = 0.15$. We find that $S \approx S_H \approx S_\ell$, and thus we can conveniently use the analytical solution from the fiber limit ($a \ll 1$) as a good approximate solution for our steady-state shape.

B. Linear theory of dewetting instability for a sandwiched sheet

To analyze the growth of perturbations along the stretching sheet, we will determine the local perturbation growth rate at certain position z_c with sheet thickness H_c. For a sheet with a constant thickness H_c without stretching, perturbations along the stretching direction and along the transverse direction grow independently in linear stability theory (the problem is separable), and the perturbations with a same wave number k in these two directions have the same growth rates $\omega_\parallel = \omega_\perp = \omega$.

Although dewetting driven by the van der Waals force has been extensively studied, a general dispersion relationship for the dewetting instability in a sandwiched liquid sheet that includes the effect of the surrounding viscosity seems to be absent from the literature. Thus, a linear analysis is performed to obtain the following dispersion relation between the perturbation growth rate ω and

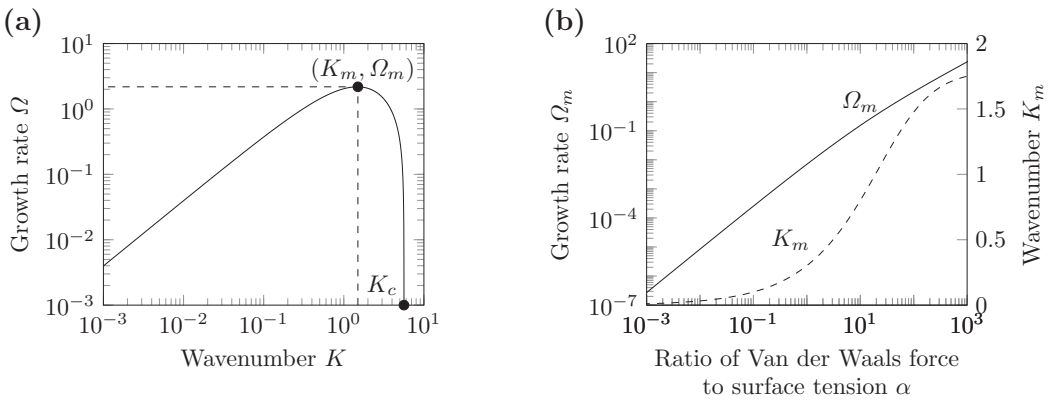

FIG. 3. Instability of a sandwiched sheet due to van der Waals force. (a) Growth rate Ω versus wave number K ($\alpha = 100$, $\eta = 1$); (b) Maximum growth rate Ω_m (solid line) and its corresponding wave number K_m (dashed line) dependent on dimensionless ratio α of van der Waals force to interfacial tension ($\eta = 1$).

the wave number k (see the derivation in the Appendix A and Ref. [14]),

$$\Omega(K, \alpha, \eta) = \frac{\alpha - \pi K^2}{2\pi K} \cdot \frac{(\sinh K - K) + \eta(\cosh K - 1)}{(\sinh K - K) + 2\eta \cosh K + \eta^2(\sinh K + K)}. \tag{5}$$

This equation is in dimensionless form, with growth rate $\Omega = \omega\mu_1 H_c/\gamma$, wave number $K = kH_c$, and viscosity ratio $\eta = \mu_2/\mu_1$. The van der Waals force is incorporated into the analysis by the Hamaker number $\mathcal{A}$, with $\alpha = \mathcal{A}/(H^2\gamma)$ denoting the ratio of the van der Waals force to the interfacial tension γ. The resulting $\Omega(K, 100, 1)$ relationship is shown in Fig. 3(a). The instability is dominated by the maximum rate Ω_m and the corresponding wave number K_m, shown as a function of α in Fig. 3(b). The growth rate Ω_m increases with α; gradually, the van der Waals force becomes dominant and drives the dewetting instability.

C. The total growth rate of perturbations in two directions

In Sec. III A, we presented an approximate solution for the stretching sheet in thermal drawing, exploiting the one-dimensional "fiber limit." Along the longitudinal direction, stretching extends the length of fluid elements at a rate S^2 due to the flow continuity, while the width and thickness are attenuated proportionate to S. Hence, the wave number of a perturbation along the stretching direction ($k_\parallel$) and the transverse direction ($k_\perp$), along with the sheet thickness (H), at any given time are related to their values at an initial position z_p and time t_p by

$$k_\parallel S^2 = k_\parallel(z_p)S^2(z_p), \quad k_\perp/S = k_\perp(z_p)/S(z_p), \quad HS = H(z_p)S(z_p). \tag{6}$$

This stretching of wave numbers changes the development of instabilities along the two directions via the dispersion relation Eq. (5) in the previous section. In order to quantitatively evaluate this effect, we adopt the approach of a total growth rate obtained by integrating local growth rate, which was suggested to study the perturbation growth of a falling liquid jet and the stability of continuous filaments [11,17]. For our stretching sheet, the total growth rate is found independently along the longitudinal ($\Phi_\parallel$) and transverse ($\Phi_\perp$) directions, and is given by

$$\begin{aligned}\Phi_\parallel(z_p, k_\parallel) &= \int_{t_p}^{t} \omega_\parallel d\tau = \frac{\gamma}{\mu_1 H_0} \int_{t_p}^{t} S(\xi)\Omega_\parallel[K_\parallel(\tau), \alpha(\tau)]d\tau \\ &= \frac{\gamma}{\mu_1 H_0 w_0} \int_{z_p}^{L} \frac{\Omega_\parallel}{S(\xi)}\left[K_\parallel(z_p)\frac{S^3(z_p)}{S^3(\xi)}, \alpha_0 S^2(\xi)\right]d\xi,\end{aligned} \tag{7a}$$

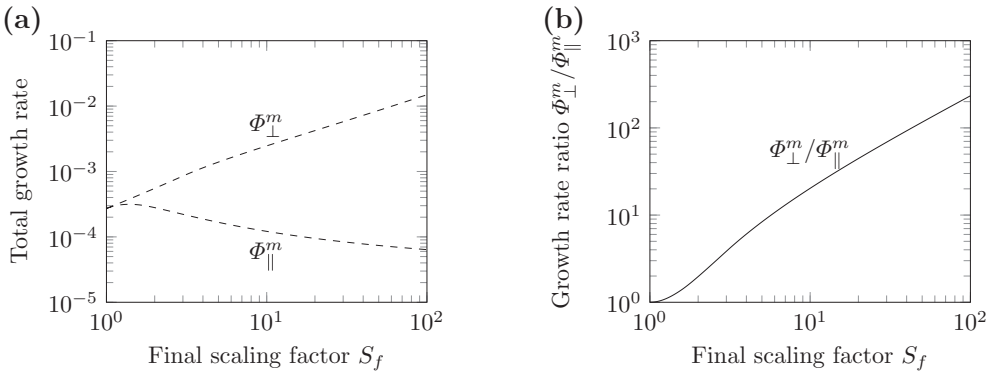

FIG. 4. Anisotropic instability arising from stretching. (a) Maximum total growth rate $\Phi_\parallel^m$, $\Phi_\perp^m$, and (b) their ratio $\Phi_\perp^m/\Phi_\parallel^m$, as a function of S_f ($\alpha_0 = 10^{-3}$, $\eta = 1$, $w_0\mu_1/\gamma = 1$, $z_p = 0$, $L/H_0 = 10^3$).

$$\Phi_\perp(z_p, k_\perp) = \int_{t_p}^{t} \omega_\perp d\tau = \frac{\gamma}{\mu_1 H_0} \int_{t_p}^{t} S(\xi)\Omega_\perp[K_\perp(\tau), \alpha(\tau)]d\tau$$
$$= \frac{\gamma}{\mu_1 H_0 w_0} \int_{z_p}^{L} \frac{\Omega_\perp}{S(\xi)}[K_\perp(z_p), \alpha_0 S^2(\xi)]d\xi. \tag{7b}$$

Here, we employ the dimensionless numbers $\alpha_0 = \mathcal{A}/(H_0^2\gamma)$ (H_0 is the thickness of the sheet at $z = 0$) and $K_\perp = k_\perp H$ and $K_\parallel = k_\parallel H$. By using the local-velocity relationship $d\tau = d\xi/w$, the time integral has been transformed into a spatial integral.

More generally, based on the two-dimensional stretching model Eq. (1) in the steady state rather than the fiber limit, the total growth rates of perturbations along the transverse and longitudinal directions are also derived in the Appendix B.

IV. NUMERICAL CALCULATION OF ANISOTROPIC INSTABILITY

Based on the mathematical model in Sec. III, we can quantitatively investigate the effect of stretching on the instability. The total growth rates of perturbations along the stretching direction $\Phi_\parallel$ and along the transversal direction $\Phi_\perp$ can be calculated by substituting the scale factor Eq. (4) and the local growth rate Eq. (5) into Eqs. (7a) and (7b) ($\alpha_0 = 10^{-3}$, $\eta = 1$, $w_0\mu_1/\gamma = 1$, $L/H_0 = 10^3$). Based on the linear theory, the amplitude of perturbation is determined by the fastest total growth rate along both directions, respectively,

$$\Phi_\parallel^m = \max[\Phi_\parallel(z_p, k_\parallel)], \quad \Phi_\perp^m = \max[\Phi_\perp(z_p, k_\perp)]. \tag{8}$$

Considering a perturbation is introduced at the starting point $z_p = 0$, $S(z_p) = 1$, the fastest total growth rate along the longitudinal directions ($\Phi_\parallel^m$) and the transversal direction ($\Phi_\perp^m$) as a function of the final scaling factor S_f are presented in Fig. 4(a). Without stretching ($S_f = 1$), the growth rate along both directions is the same ($\Phi_\parallel^m = \Phi_\perp^m$), recovering the isotropic instability of dewetting. However, as stretching starts to play a role ($S_f > 1$), an anisotropic instability phenomenon appears ($\Phi_\parallel^m < \Phi_\perp^m$) and becomes more striking at larger S_f.

Along the longitudinal stretching direction, $\Phi_\parallel^m$ obviously decreases with the increased S_f. According to Eq. (7a),

$$K_\parallel = K_\parallel(z_p)S^3(z_p)/S^3 \sim K_\parallel(z_p)S_f^{-3}, \tag{9}$$

the wave number of the perturbation decays dramatically with stretching, up to three orders of magnitude for $S_f \sim 10$. This significant reduction of the wave number to $K_\parallel < K_c$ correspondingly leads to a diminished growth rate, as seen in Fig. 3(a), and the possible occurrence of breakup

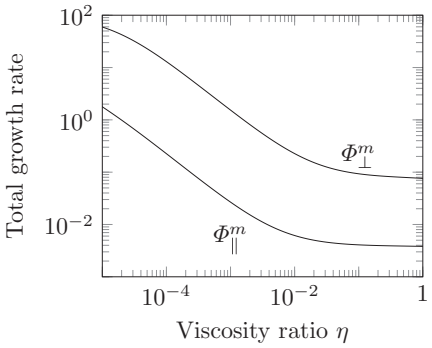

FIG. 5. Anisotropic instability associated with the viscosity ratio ($\alpha_0 = 10^{-2}, S_f = 10,\ w_0\mu_1/\gamma = 1, z_p = 0, L/H_0 = 10^3$).

is delayed. So the longitudinal instability can be suppressed by the stretching, although the destabilization effect of van der Waals force remains.

In contrast, along the transverse direction, $\Phi_\perp^m$ is substantially enhanced. According to Eq. (7b),

$$\alpha = \alpha_0 S^2 \sim \alpha_0 S_f^2, \tag{10}$$

the α factor is increased by up to two orders of magnitude for $S_f \sim 10$, although $K_\perp$ keeps constant. From Fig. 3(b), the enhancement of α correspondingly results in an increase of $\Phi_\perp^m$. In other words, as the thickness of the sheet H is reduced by stretching, the van der Waals force becomes much more influential and further accelerates the growth of instabilities. Consequently, the transverse instability is dramatically enhanced.

To further demonstrate the contrast between the enhanced instability $\Phi_\perp^m$ and the suppressed instability $\Phi_\parallel^m$, we show their ratio $\Phi_\perp^m/\Phi_\parallel^m$ as a function of S_f in Fig. 4(b), which can exceed two orders of magnitude. According to the similar analysis [13,17], breakup starts to occur once the fastest total growth rate reaches beyond a certain critical value Φ_{cri},

$$\max(\Phi_\parallel^m, \Phi_\perp^m) > \Phi_{\text{cri}}. \tag{11}$$

The total growth rate along the transversal direction $\Phi_\perp^m$ is larger and consequently reaches the critical value Φ_{cri} first,

$$\Phi_\perp^m > \Phi_{\text{cri}} > \Phi_\parallel^m. \tag{12}$$

Under this condition, breakup occurs exclusively along the transverse direction, while continuity is preserved along the longitudinal direction, resulting in AISVS.

Moreover, the effect of viscosity ratio on anisotropic instability is studied by following the similar calculation steps, i.e., by substituting the scale factor Eq. (4) and the local growth rate Eq. (5) into Eqs. (7a) and (7b) together with Eq. (8). The total growth rates along the longitudinal directions ($\Phi_\parallel^m$) and the transversal direction ($\Phi_\perp^m$) versus viscosity ratio η are shown in Fig. 5 ($\alpha_0 = 10^{-2}, S_f = 10,\ w_0\mu_1/\gamma = 1, z_p = 0, L/H_0 = 10^3$). A smaller viscosity ratio (via a smaller μ_2 and a fixed μ_1) leads to faster growth for both $\Phi_\perp^m$ and $\Phi_\parallel^m$, but the anisotropic instability remains ($\Phi_\perp^m > \Phi_\parallel^m$).

In practice, the perturbations can be introduced at any point along the stretching direction [$z_p \in (0, L)$], instead of the starting point ($z_p = 0$). Along the transverse direction, $\Phi_\perp^m$ still increases with S_f, similar to the case of $z_p = 0$. Along the longitudinal stretching direction, $\Phi_\parallel^m$ may actually rise with S_f as well, since the introduced perturbations could be near the end of stretching area ($z_p \to L$) where the sheet has already become very thin. However, $\Phi_\perp^m > \Phi_\parallel^m$ still holds to induce AISVS.

TABLE I. Typical physical parameters during thermal drawing [11,13].

Polymer/glass/polymer	μ_1(Pas)	μ_2(Pas)	η	γ (Nm^{-1})	$\mathcal{A}$ (J)	L(m)	w_0 (ms^{-1})	S_f
PES/As_2Se_3/PES	10^5	10^5	1	10^{-1}	10^{-17}	0.1	3×10^{-6}	20
PSU/Se/PSU	10^5	1	10^{-5}	10^{-1}	10^{-17}	0.1	3×10^{-6}	20

V. APPLICATION FOR THERMAL DRAWING OF FIBERS

We now compare our theoretical predictions with experimental results for AISVS. AISVS is observed during thermal drawing for a polymer/glass/polymer fiber structure, polyethersulfone (PES)/As_2Se_3/PES or polysulfones (PSU)/Se/PSU (physical parameters listed in the Table I).

For PES/As_2Se_3/PES and PSU/Se/PSU, the relationship between $\Phi_\perp^m$ and the initial thickness H_0 [Fig. 6(a)] is calculated from Eq. (8) for perturbations introduced at any point $z_p \in (0, L)$ along the stretching direction. For both cases, as H_0 deceases the van der Waals force induces a faster instability and a larger $\Phi_\perp^m$. A less viscous Se sheet ($\eta = 10^{-5}$) has a larger $\Phi_\perp^m$ than that of a high-

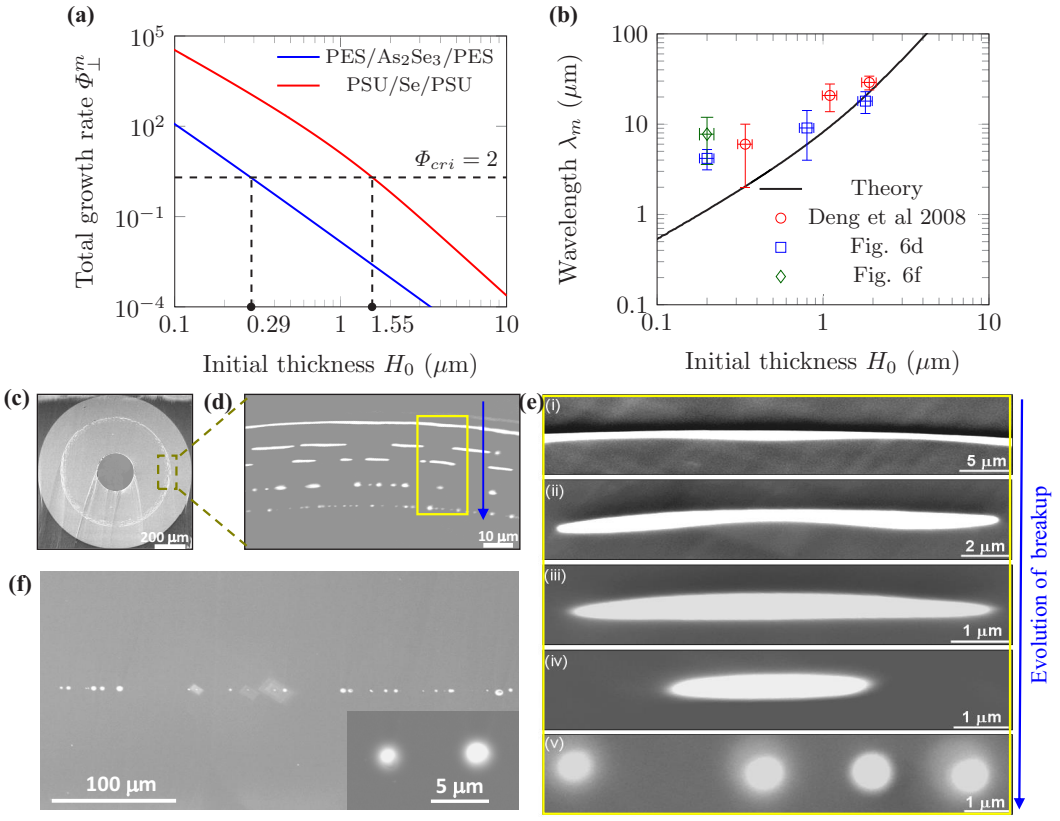

FIG. 6. Fiber applications. (a), (b) Theoretical predictions agreeing with experimental data. (a) $\Phi_\perp^m$ for PES/As_2Se_3/PES and PSU/Se/PSU, the dashed line for $\Phi_{\text{cri}} = 2$. (b) For PSU/Se/PSU, the predicted wavelength agreeing with the measured wavelength (Deng et al 2008: [11]). (c)–(e) SEM imaging for evolution of instability and breakup for five final targeted film thickness of 300, 170, 90, 40, and 10 nm, respectively. (f) SEM imaging for a ribbon-fiber cross-section for a final targeted 10-nm-thick film, and its inset presenting the circular shapes. Dark color for PSU, bright color for Se, and arrow indicating the decreased targeted thickness.

viscosity As_2Se_3 sheet ($\eta = 1$). The criterion for AISVS is $\Phi_{\perp}^{m} > \Phi_{\text{cri}}$, where $\Phi_{\text{cri}} = 2$ is fixed since the amplitude of instability grows exponentially with time. As indicated in Fig. 6(a), the breakup of As_2Se_3 and Se sheet may occur for $H_0 < 0.29$ and 1.55 μm, respectively. This prediction, which implies that the final thickness of As_2Se_3 and Se sheet subjected to AISVS ($S_f = 20$) is below 14.5 and 77.5 nm, agrees well with the observed AISVS for As_2Se_3 and Se below 10 and 100 nm, respectively [11].

Moreover, for PSU/Se/PSU fiber, we further predict the dependency of the instability wavelength on the thickness H_0 in Fig. 6(b). The theoretical wavelength (black line) is obtained from $\lambda_m = 2\pi S(z_m)/(k_m S_f)$, since perturbations with wave number k_m introduced at z_m have the fastest growth rate $\Phi_{\perp}^{m}$. The experimental wavelength (λ_{exp})is measured by averaging the spacings of Se filament arrays in scanning electronic microscopic (SEM) images of fiber cross sections, and the data set (circles) in Fig. 6(b) from our previous experiments [11] ($\lambda_{\text{exp}} = 6$, 20.8 and 29 μm for $H_0 = 0.34$, 1.1 and 1.9 μm, respectively) exhibits a remarkable agreement with the theory.

To further investigate the instability evolution and validate our theory, we designed a preform containing five concentric Se films of decreasing thicknesses ($H_0 = 6$, 3.4, 1.8, 0.8, and 0.2 μm) to target the final film thickness (300, 170, 90, 40, and 10 nm with $S_f = 20$) and carried out another thermal draw (details in Appendix C) [19]. SEM micrographs of a fiber cross section [Figs. 6(c) and 6(d)] show the instability evolution and eventual breakup of films (bright color for Se and dark color for PSU), and a close-up view with a higher spatial resolution [Fig. 6(e)] clearly reveals the instability morphology as the targeted thickness is decreased down to the sub-micron scale. For a large $H_0 = 6$ μm [Fig. 6(e) (i)], the instability develops by amplifying sinusoidal perturbations, forming a wavy pattern. For a thinner $H_0 = 3.4$ μm [Fig. 6(e) (ii)], instability has grown much further, resulting in film rupture and generating many slender segments. As H_0 is reduced to 1. 8 and 0.8 μm, long slender segments gradually transform into short segments [Fig. 6(e) (iii) and (iv)]. Eventually, for the thinnest $H_0 = 0.2$ μm, the target 10-nm-thick film has completely broken up into filaments with circular cross-sections [Fig. 6(e) (v)]. More quantitatively, the instability wavelength [squares in Fig. 6(b)] from this experiment ($\lambda_{\text{exp}} = 4.18$, 9.08, and 18.01 μm for $H_0 = 0.2$, 0.8, 1.8 μm, respectively) agrees with the theory as well.

AISVS can exist in ribbon fibers as well as cylindrical fibers, since the circumferential curvature (much larger than the layer thickness) is unlikely to be relevant for filamentation. A ribbon fiber was drawn from a flat PSU/Se/PSU preform, and SEM micrographs [Fig. 6(f)] indicate the breakup for a targeted 10-nm-thick film. Again, the measured instability wavelength [the diamond symbol in Fig. 6(b)] is comparable with the theoretical prediction.

VI. DISCUSSION AND OUTLOOK

Our theoretical predictions agree well with our experimental observations, in terms of both the breakup thickness and the instability wavelength. Nevertheless, there are many opportunities for future work to further explore AISVS in theory, simulation, experiment, and application. First, a general theory should include nonlinear effects arising from late stages of the instability, inertial contributions, non-Newtonian behaviors of the molten glass, and the exact necking effect (instead of the analytical "fiber limit" approximation). These nonlinear effects might be responsible for the noticeable deviation between theory and experiment for a final targeted thickness around 10 nm ($H_0 = 0.2$ μm) in Fig. 6(b). Second, direct numerical simulation might provide greater insight into instability evolution along the transverse direction for quantitative comparison with the observed patterns in Fig. 6(e), although this involves a challenging multiscale simulation spanning several orders of magnitude (millimeters in length and micrometer or nanometers in thickness). Third, the final stage of instability and breakup was observed in this work by static SEM images of the fiber cross section, but a real-time visualization of a stretching viscous sheet would resolve the full dynamical evolution of AISVS. Last, more sophisticated nanostructures might be achieved through filamentation in two adjacent sheets or three-layer sandwiched sheets, and by utilizing the available toolbox of various materials combination (such as semiconductors, metals, and polymers)

compatible with thermal drawing, one could increase the already-impressive range of functional nanodevices that can be realized in either single fibers or mass-produced in large-scale textiles [20–22].

VII. CONCLUSION

In summary, we propose a physical mechanism of AISVS by taking into account both van der Waals forces and stretching. The stretching plays a key role in this anisotropic instability by enhancing the transverse instability and suppressing the longitudinal instability, resulting in filament formation. Moreover, the theoretical predications agree well with the experimental data. These results might provide guidance to design more sophisticated functional microdevices–nanodevices in fibers and textiles.

ACKNOWLEDGMENTS

D.D. acknowledges Prof. H. A. Stone for the initial idea of the van der Waals force acting with stretching, N. Orf and S. Danto for helping fiber drawing, and Steve Kooi for SEM imaging. We acknowledge the anonymous reviewers for the constructive comments. This work was supported by the National Young Thousand Talent Program in China and startup from Fudan University, the China Postdoctoral Science Foundation, and by the Materials Research Science and Engineering Center Program of the National Science Foundation under Award DMR-1419807.

APPENDIX A: LINEAR DEWETTING INSTABILITY

For the sheet with a constant thickness H_c without stretching, perturbations along the longitudinal direction and along the transverse direction are assumed to grow independently, and the perturbations with the same wave number k in these two directions are assumed to have the same growth rates $\omega_{\parallel} = \omega_{\perp} = \omega$. Thus, we can consider a two-dimensional thin sheet in $y - z$ plane (or in x-y plane) with constant thickness H_c sandwiched between two fluids, and Van der Waals force is introduced by the potential energy per unit area $V(H_c) = -\mathcal{A}/(12\pi H_c^2)$ with a Hamaker constant $\mathcal{A}$. The governing equations (the Reynolds number $\mathrm{Re} \ll 1$) and interfacial boundary conditions are

$$\nabla \cdot \boldsymbol{\sigma}_j = 0, \quad \nabla \cdot \boldsymbol{u}_j = 0, \tag{A1a}$$

$$\boldsymbol{u}_i = \boldsymbol{u}_{i+1}, \quad \boldsymbol{n}_i \cdot \boldsymbol{\sigma}_i \cdot \boldsymbol{t}_i = \boldsymbol{n}_i \cdot \boldsymbol{\sigma}_{i+1} \cdot \boldsymbol{t}_i, \tag{A1b}$$

$$\boldsymbol{n}_i \cdot (\boldsymbol{\sigma}_{i+1} - \boldsymbol{\sigma}_i) \cdot \boldsymbol{n}_i = \gamma_i \kappa_i - \frac{dV(H_c)}{dH_c}. \tag{A1c}$$

Here the subscript $j = 1, 2$ and 3 for the fluid of three layers, $\boldsymbol{u}_j$ is velocity, p_j pressure, μ_j viscosity, and $\boldsymbol{\sigma}_j = -p_j \boldsymbol{\delta} + \mu_j[\nabla \boldsymbol{u}_j + (\nabla \boldsymbol{u}_j)^T]$ viscous stress tensor. The subscript $i = 1, 2$ for two interfaces, γ_i is surface tension, κ_i mean curvature, $\boldsymbol{n}_i$ and $\boldsymbol{t}_i$ unit normal vectors and unit tangential vectors at the interface.

Without perturbations, the three-layer thin liquid sheet is assumed to flow downstream with a uniform velocity w as a plug flow. When this steady state is disturbed by small perturbations, the following linearized governing equations and boundary conditions for perturbations can be obtained

$$\nabla \tilde{p}_j = \mu_j \nabla^2 \tilde{\boldsymbol{u}}_j, \tag{A2}$$

$$\nabla \cdot \tilde{\boldsymbol{u}}_j = 0, \tag{A3}$$

$$\tilde{\boldsymbol{u}}_i \cdot \bar{\boldsymbol{n}}_i = \tilde{\boldsymbol{u}}_{i+1} \cdot \bar{\boldsymbol{n}}_i = \frac{\partial \tilde{Y}_i}{\partial t}, \tag{A4}$$

$$\tilde{\boldsymbol{u}}_i \cdot \bar{\boldsymbol{t}}_i = \tilde{\boldsymbol{u}}_{i+1} \cdot \bar{\boldsymbol{t}}_i, \tag{A5}$$

$$\bar{\boldsymbol{n}}_i \cdot \tilde{\boldsymbol{\sigma}}_i \cdot \bar{\boldsymbol{t}}_i = \bar{\boldsymbol{n}}_i \cdot \tilde{\boldsymbol{\sigma}}_{i+1} \cdot \bar{\boldsymbol{t}}_i, \tag{A6}$$

$$\bar{\boldsymbol{n}}_i \cdot (\tilde{\boldsymbol{\sigma}}_{i+1} - \tilde{\boldsymbol{\sigma}}_i) \cdot \bar{\boldsymbol{n}}_i = -\gamma_i \frac{\partial^2 \tilde{Y}_i}{\partial z^2} + \frac{\mathcal{A}\tilde{H}_c}{2\pi H_c^4}, \tag{A7}$$

where $\tilde{\kappa}_i = \boldsymbol{\nabla} \cdot \tilde{\boldsymbol{n}}_i = -\partial^2 \tilde{Y}_i / \partial z^2$ is used in the boundary condition Eq. (A7), the bar indicates the variables in the steady state and the tilde the corresponding perturbations. The solution to this problem can be sought under the normal mode assumption for the perturbations, such as $\tilde{Y}_i = \epsilon_i \exp(\omega t + ikz)$, $\tilde{\boldsymbol{u}}_j = \tilde{\boldsymbol{U}}_j(y)\exp(\omega t + ikz)$. Thus, the general solutions are

$$\tilde{\boldsymbol{u}}_j = \begin{bmatrix} ik\left(c_j^1 e^{ky} + c_j^2 e^{-ky} + c_j^3 y e^{ky} + c_j^4 y e^{-ky}\right) \\ -\left(kc_j^1 + c_j^3 + kyc_j^3\right)e^{ky} - \left(-kc_j^2 + c_j^4 - kyc_j^4\right)e^{-ky} \end{bmatrix} e^{(\omega t + ikz)} \tag{A8}$$

and

$$\tilde{p}_j = 2\mu_j ik\left(c_j^3 e^{ky} + c_j^4 e^{-ky}\right)e^{(\omega t + ikz)}. \tag{A9}$$

Substituting these general solutions into the boundary conditions Eqs. (A4)–(A7) yields the equation set about the integral constants $c_j^1, c_j^2, c_j^3, c_j^4$. In addition, the velocity and pressure should be finite at the outer surfaces of fluids 1 and 3. Since the thickness of outer fluids 1 and 3 are much larger than the thin sheet thickness H_c, these boundary conditions are like to ones that perturbations are finite $y \to -\infty$ and $y \to \infty$, i.e., $c_2^1 = c_4^1 = c_1^3 = c_3^3 = 0$. There is non-zero solutions of integral constants in the equation set, so its coefficient matrix should be singular to give the dispersion relation between growth rate ω and wave number k.

The liquid sheet in same surrounding fluids is studied ($\mu_1 = \mu_3$, $\rho_1 = \rho_3$, $\gamma_1 = \gamma_2 = \gamma$). There are sinuous mode ($\epsilon_1 = \epsilon_2$) and varicose mode ($\epsilon_1 = -\epsilon_2$) instability. The perturbation of the sheet thickness is given by $\tilde{H}_c = \epsilon_1 - \epsilon_2$. Then, the varicose mode is considered in which the van der Waals forces play a role as shown in Eq. (A7), and the dispersion relation is simplified to

$$\begin{vmatrix} 1 & -\frac{H_c}{2} & 1 & -\frac{H_c}{2} \\ k & \left(1 - \frac{kH_c}{2}\right) & -k\coth\left(\frac{kH_c}{2}\right) & 1 + \frac{kH_c}{2}\tanh\left(\frac{kH_c}{2}\right) \\ \mu_1 k^2 & \mu_1 k\left(1 - \frac{kH_c}{2}\right) & \mu_2 k^2 & \mu_2 k\left[-\tanh\left(\frac{kH_c}{2}\right) - \frac{kH_c}{2}\right] \\ -ik^2\left(2\mu_1 + \frac{\gamma_{eff}k}{\omega}\right) & ik\frac{kH_c}{2}\left(2\mu_1 + \frac{\gamma_{eff}k}{\omega}\right) & 2\mu_2 ik^2\coth\left(\frac{kH_c}{2}\right) & -\mu_2 H_c ik^2\tanh\left(\frac{kH_c}{2}\right) \end{vmatrix} = 0,$$

$$\Longrightarrow \omega = -\frac{\gamma_{eff}k}{2}\frac{\mu_2(\cosh(kH_c) - 1) + \mu_1(\sinh(kH_c) - kH_c)}{\mu_2^2[\sinh(kH_c) + kH_c] + 2\mu_1\mu_2\cosh(kH_c) + \mu_1^2[\sinh(kH_c) - kH_c]}, \tag{A10}$$

where $\gamma_{\text{eff}} = \gamma - \frac{\mathcal{A}}{k^2\pi H_c^4}$ is the effective surface tension including the van der Waals force. This dispersion relation Eq. (A10) is identical to Liang's result [14], and can be nondimensionalized to the Eq. (5) in the paper.

APPENDIX B: DERIVATIONS OF TOTAL GROWTH RATES OF PERTURBATIONS WITH 2D STRETCHING MODEL

In the Sec. III A, the lateral shape solutions of the stretching sheet in the steady state in 2D stretching model at the aspect ratio $a = 0.15$ and the 1D "fiber limit" model are shown in the Fig. 2. Considering the small difference of the these two solutions, the lateral shape solution in the 1D "fiber limit" model is used as the approximate solution for simplicity in the above study. In this Appendix, the 2D stretching model will be used for more information.

As mentioned above in Sec. III A, with the 2D stretching model, the attenuation rates of thickness $S_H = H_0/H$ and width $S_\ell = \ell_0/\ell$ are not equal to each other $S_H \neq S_\ell$. Then, Eqs. (6) of the wave number of perturbation along the stretching direction ($k_\parallel$), that along the transverse direction ($k_\perp$),

and the sheet thickness (H) become

$$k_\parallel S_H S_\ell = k_\parallel(z_p) S_H(z_p) S_\ell(z_p), \quad k_\perp / S_\ell = k_\perp(z_p)/S_\ell(z_p), \quad H S_H = H(z_p) S_H(z_p). \tag{B1}$$

Consequently, the total growth rate along the longitudinal stretching direction ($\Phi_\parallel$) and transverse direction ($\Phi_\perp$) with Eqs. (B1) are

$$\Phi_\parallel(z_p, k_\parallel) = \int_{t_p}^{t} \omega_\parallel d\tau = \frac{\gamma}{\mu_1 H_0} \int_{t_p}^{t} S_H(\xi) \Omega_\parallel[K_\parallel(\tau), \alpha(\tau)] d\tau$$
$$= \frac{\gamma}{\mu_1 H_0 w_0} \int_{z_p}^{L} \frac{1}{S_\ell(\xi)} \Omega_\parallel \left[K_\parallel(z_p) \frac{S_H^2(z_p) S_\ell(z_p)}{S_H^2(\xi) S_\ell(\xi)}, \alpha_0 S_H^2(\xi) \right] d\xi, \tag{B2a}$$

$$\Phi_\perp(z_p, k_\perp) = \int_{t_p}^{t} \omega_\perp d\tau = \frac{\gamma}{\mu_1 H_0} \int_{t_p}^{t} S_H(\xi) \Omega_\perp[K_\perp(\tau), \alpha(\tau)] d\tau$$
$$= \frac{\gamma}{\mu_1 H_0 w_0} \int_{z_p}^{L} \frac{1}{S_\ell(\xi)} \Omega_\perp \left[K_\perp(z_p) \frac{S_H(z_p) S_\ell(\xi)}{S_\ell(z_p) S_H(\xi)}, \alpha_0 S_H^2(\xi) \right] d\xi. \tag{B2b}$$

Compared to Eqs. (7a) and (7b) in the 1D "fiber limit" model, Eqs. (B2a) and (B2b) in the 2D stretching model, especially the wave numbers $K_\parallel$ and $K_\perp$, are more complicated. Using the approximate solution in the 1D "fiber limit," the underlying mechanism of the anisotropic instability phenomenon can be revealed more straightforwardly.

APPENDIX C: THERMAL DRAWING FOR FIBERS

The preform was composed by five concentric Se films with the graded thicknesses embedded in PSU polymer matrix, and was consolidated under vacuum for approximately one hour at 220 °C. Then the preform was drawn in a conventional optical fiber draw tower at 260 °C. A feeding process controllably introduced the preform into the furnace with downfeed speed of 0.003 mm s^{-1}, and a capstan pulled the resulting fiber from the preform was 0.1 m min^{-1} were used. Consequently, the drawing parameters were fixed to keep a constant draw-down ratio of about 20 between the feature sizes of the initial preform and final fiber. SEM samples of a fiber were prepared by ion polishing with a JEOL cross-section polisher, and subsequently the micrographs were taken with a JEOL SEM.

[1] A. Oron, S. H. Davis, and S. G. Bankoff, Long-scale evolution of thin liquid films, Rev. Mod. Phys. **69**, 931 (1997).

[2] R. V. Craster and O. K. Matar, Dynamics and stability of thin liquid films, Rev. Mod. Phys. **81**, 1131 (2009).

[3] H. B. Squire, Investigation of the instability of a moving liquid film, Br. J. Appl. Phys. **4**, 167 (1953).

[4] G. I. Taylor, The dynamics of thin sheets of fluid. III. Disintegration of fluid sheets, Proc. R. Soc. London A **253**, 313 (1959).

[5] N. M. Ribe, Bending and stretching of thin viscous sheets, J. Fluid Mech. **433**, 135 (2001).

[6] G. Pfingstag, B. Audoly, and A. Boudaoud, Linear and nonlinear stability of floating viscous sheets, J. Fluid Mech. **683**, 112 (2011).

[7] N. M. Ribe, M. Habibi, and D. Bonn, Liquid rope coiling, Annu. Rev. Fluid Mech. **44**, 249 (2012).

[8] S. Srinivasan, Z. Wei, and L. Mahadevan, Wrinkling instability of an inhomogeneously stretched viscous sheet, Phys. Rev. Fluids **2**, 074103 (2017).

[9] G. Reiter, Dewetting of Thin Polymer Films, Phys. Rev. Lett. **68**, 75 (1992).
[10] G. Reiter, Unstable thin polymer films: Rupture and dewetting processes, Langmuir **9**, 1344 (1993).
[11] D. Deng, N. D. Orf, A. F. Abouraddy, A. M. Stolyarov, J. D. Joannopoulos, H. A. Stone, and Y. Fink, In-fiber semiconductor filament arrays, Nano Lett. **8**, 4265 (2008).
[12] D. Deng, N. D Orf, S. Danto, A. F. Abouraddy, J. D. Joannopoulos, and Y. Fink, Processing and properties of centimeter-long, in-fiber, crystalline-selenium filaments, Appl. Phys. Lett. **96**, 023102 (2010).
[13] D. Deng, J. Nave, X. Liang, S. G. Johnson, and Y. Fink, Exploration of in-fiber nanostructures from capillary instability, Opt. Express **19**, 16273 (2011).
[14] X. Liang, Modeling of fluids and waves with analytics and numerics, Ph.D. thesis, Massachusetts Institute of Technology, 2013.
[15] S. Shabahang, J. J. Kaufman, D. S. Deng, and A. F. Abouraddy, Observation of the Plateau-Rayleigh capillary instability in multi-material optical fibers, Appl. Phys. Lett. **99**, 161909 (2011).
[16] J. J. Kaufman, G. Tao, S. Shabahang, E. Banaei, D. S. Deng, X. Liang, S. G. Johnson, Y. Fink, and A. F. Abouraddy, Structured spheres generated by an in-fibre fluid instability, Nature **487**, 463 (2012).
[17] A. Javadi, J. Eggers, D. Bonn, M. Habibi, and N. M. Ribe, Delayed Capillary Breakup of Falling Viscous Jets, Phys. Rev. Lett. **110**, 144501 (2013).
[18] B. Scheid, S. Quiligotti, B. Tran, and H. A. Stone, Lateral shaping and stability of a stretching viscous sheet, Eur. Phys. J. B **68**, 487 (2009).
[19] D. S. Deng, In-fiber semiconductor filament arrays, Ph.D. thesis, Massachusetts Institute of Technology, 2010.
[20] A. F. Abouraddy, M. Bayindir, G. J. Benoit, S. Hart, K. Kuriki, N. D. Orf, O. Shapira, F. Sorin, B. Temelkuran, and Y. Fink, Toward multimaterial multifunctional fibres that see, hear, sense, and communicate, Nat. Mater. **6**, 336 (2007).
[21] C. Markos, J. C. Travers, A. Abdolvand, B. J. Eggleton, and O. Bang, Hybrid photonic-crystal fiber, Rev. Mod. Phys. **89**, 045003 (2017).
[22] M. Rein, V. D. Favrod, C. Hou, T. Khudiyev, A. Stolyarov, J. Cox, C. Chung, C. Chhav, M. Ellis, J. Joannopoulos, and Y. Fink, Diode fibres for fabric-based optical communications, Nature **560**, 214 (2018).